



Batteries Hot Paper

How to cite: *Angew. Chem. Int. Ed.* **2021**, *60*, 11835–11840

International Edition: doi.org/10.1002/anie.202103052

German Edition: doi.org/10.1002/ange.202103052

Novel Lamellar Tetrapotassium Pyromellitic Organic for Robust High-Capacity Potassium Storage

Qingguang Pan, Yongping Zheng, Zhaopeng Tong, Lei Shi, and Yongbing Tang*

Abstract: Redox-active organics are investigation hotspots for metal ion storage due to their structural diversity and redox reversibility. However, they are plagued by limited storage capacity, sluggish ion diffusion kinetics, and weak structural stability, especially for K^+ ion storage. Herein, we firstly reported the lamellar tetrapotassium pyromellitic (K_4PM) with four active sites and large interlayer distance for K^+ ion storage based on a design strategy, where organics are constructed with the small molecular mass, multiple active sites, fast ion diffusion channels, and rigid conjugated π bonds. The K_4PM electrode delivers a high capacity up to 292 mAh g^{-1} at 50 mA g^{-1} , among the best reported organics for K^+ ion storage. Especially, it achieves an excellent rate capacity and long-term cycling stability with a capacity retention of $\approx 83\%$ after 1000 cycles. Incorporating in situ and ex-situ techniques, the K^+ ion storage mechanism is revealed, where conjugated carboxyls are reversibly rearranged into enolates to stably store K^+ ions. This work sheds light on the rational design and optimization of organic electrodes for efficient metal ion storage.

Lithium-ion batteries (LIBs) have dominated the global energy storage market for portable electronics, electric vehicles and grid-scale storage in the past decades.^[1] Nevertheless, the resource scarcity in the Earth's crust (0.0017 wt%) and maldistribution of lithium have become significant obstacles to impede the sustainable advance of LIBs.^[2] Noteworthily, potassium-ion batteries (PIBs) with the similar energy storage mechanism and adjacent redox couple to LIBs (-2.93 V for K^+/K vs. -3.04 V for Li^+/Li) have been one of the research hotspots benefiting from the abundant reserves of potassium resource (2.09 wt%).^[3] Nevertheless, the exploration of PIBs is still in its infancy, and the key

challenge consists of searching for suitable electrode materials.

Recently, extensive candidates for K^+ ion storage have been investigated including intercalation-type carbonaceous materials,^[4] and Mxenes,^[5] intercalation and conversion-type chalcogenide,^[6] alloy-type metals^[7] and phosphide,^[8] which all inevitably suffer from the distinct volume expansion ascribed to the insertion of large-sized K^+ ions, resulting in the battery capacity fading.^[9] Therefore, it remains a challenge to develop high efficient electrode materials. Recently, organics have attracted much attention for their structural diversity, flexible designability, and redox reversibility.^[10] For example, conjugated carbonyl compounds,^[11] nitroaromatics,^[12] azo,^[13] polymers,^[14] covalent organic frameworks,^[15] metal-organic frameworks,^[16] etc., have been proved can reversibly manipulate molecular structures to accommodate large K^+ ions without structural collapse.^[17] However, they still need to be further optimized on account of the finite ion storage capacity, sluggish diffusion kinetics of K^+ ions, and poor structural robustness.^[18] To address the above issues, organics for metal ion storage should present the following properties. Firstly, to achieve the high specific capacity, organics should possess small molecular mass and rich active sites as many as possible. Secondly, if they could contribute the fast ion diffusion channels, the ion diffusion barriers for K^+ ion storage can be decreased, resulting in the fast rate capacity. Further, the structural stability could be enhanced, if the organic molecules contained rigid conjugated π bond groups.

Based on the above strategy, we firstly design and synthesize a lamellar tetrapotassium pyromellitic (K_4PM) via a one-step and scalable method. In this case, we choose pyromellitic acid (PMA) as the precursor owing to its small molecular mass, four K^+ ion storage sites, convenient ion diffusion routes, and rigid conjugated π bonds from the benzene ring. Accordingly, the as-prepared layered K_4PM achieves a high theoretical capacity, fast K^+ ion diffusion kinetics and excellent robustness for K^+ ion storage due to its four conjugated carboxylate groups as active sites and a large interlayer distance than conventional graphite materials. Eventually, the above contributions synergistically boost the potassium storage with a high specific capacity of 292 mAh g^{-1} , good rate performance and excellent long cycling stability with a capacity retention of $\approx 83\%$ after 1000 cycles, among the best results of K-organic batteries.

Typically, the four carboxylic acids in the precursor react with KOH through a neutral reaction, where four H^+ ions of carboxylic acid in PMA can be substituted by four K^+ ions, forming the K_4PM , as displayed in Figure 1 a. X-ray diffraction (XRD) characterizations of the as-prepared sample and precursor were performed, where peaks of as-prepared

[*] Dr. Q. G. Pan, Dr. Y. P. Zheng, Z. P. Tong, L. Shi, Prof. Y. B. Tang
Functional Thin Films Research Center, Shenzhen Institute of
Advanced Technology, Chinese Academy of Sciences
Shenzhen 518055 (China)
E-mail: tangyb@siat.ac.cn

Prof. Y. B. Tang
School of Chemical Science, University of Chinese Academy of
Sciences
Beijing 100049 (China)
and
Key Laboratory of Advanced Materials Processing & Mold, Ministry
of Education, Zhengzhou University
Zhengzhou 450002 (China)

Supporting information and the ORCID identification number(s) for
the author(s) of this article can be found under:
<https://doi.org/10.1002/anie.202103052>.

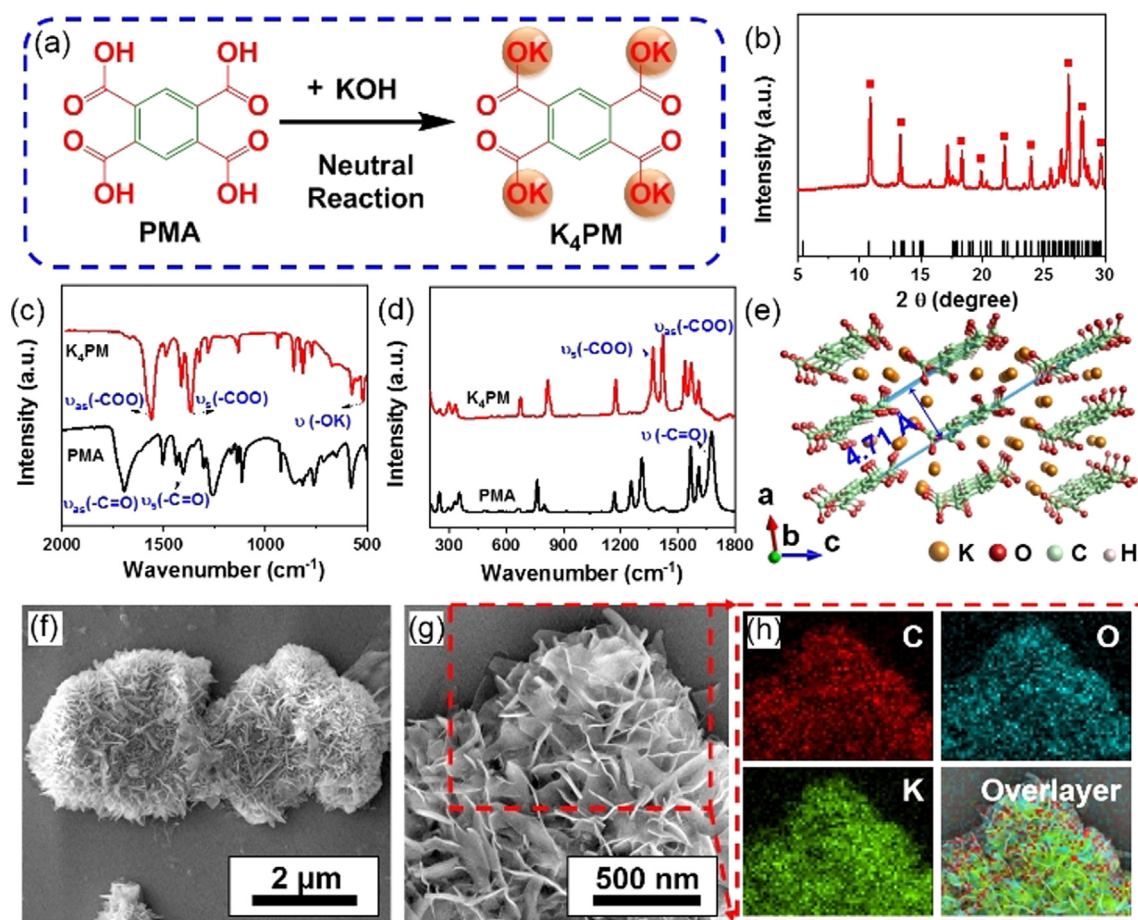


Figure 1. a) Synthesis route of K_4PM . b) XRD pattern of K_4PM . Vertical dark lines indicate the simulation diffraction peaks. c) FT-IR and d) Raman spectra of PMA and K_4PM . e) The crystalline structure of K_4PM . f, g) SEM images of K_4PM and h) corresponding EDS mapping images.

sample match well with simulation results of K_4PM and are obviously different PMA (Figure 1b and Figure S1 in Supporting Information), especially for the main characteristic peaks of 10.9° , 13.4° , 18.4° , 21.8° , 24.0° , and 27.0° , indicating the high crystallographic forms of a triclinic lattice. Figure 1c manifests the Fourier transform infrared (FT-IR) spectra of as-prepared K_4PM and PMA. The PMA exhibits the asymmetric and symmetric stretching vibrations of $-C=O$ (i.e., $\nu_{as}(-C=O)$) at 1690 cm^{-1} and $\nu_s(-C=O)$ at 1406 cm^{-1} , which belong to the characteristic of the carboxylic acid group.^[19] As for the synthesized K_4PM , the emerged peaks at 1561 , 1367 , and 522 cm^{-1} match well with $\nu_{as}(-COO)$, $\nu_s(-COO)$, and the $-OK$ out-of-plane bending vibration (i.e., $\nu(-OK)$), while the peaks of PMA at 1690 and 1406 cm^{-1} disappear.^[19] Raman spectra (Figure 1d) also show two peaks at 1567 and 1370 cm^{-1} corresponding to the $\nu_{as}(-COO)$ and $\nu_s(-COO)$ of K_4PM , respectively, obviously different from the PMA.^[19,20] Accordingly, the crystalline structure of K_4PM is simulated as demonstrated in Figures 1e and S2, which features the layered structure with an interlayer space of 4.71 \AA , much larger than that of graphite materials (3.35 \AA),^[21] possibly beneficial for the large ion storage. Moreover, the typical scanning electron microscope (SEM) images of K_4PM exhibit the lamellar structure (Figures 1f and g) and corresponding energy dispersive spectroscopy (EDS) mapping images further

identify the uniform distribution of C, O, and K elements (Figure 1h). According to the Brunauer-Emmett-Teller (BET) measurement, the synthesized K_4PM has a specific surface area ($31.90\text{ m}^2\text{ g}^{-1}$) and a large mesoporous volume (Figure S3), in favor of the fast ion diffusion.^[22]

The electrochemical kinetics and performances of K_4PM were investigated with a K foil as the counter electrode within coin-type cells. Based on the relationship: $i = av^b$, the contributions of the surface pseudocapacitive and diffusion behaviors can be assessed by CV curves at different scan rates (Figure 2a), where a and b are tunable values, when the value of b is 0.5, representing the diffusion-controlled process, once the value of b attains 1.0, meaning the surface capacitive-controlled process.^[23] Figure 2b shows that the value of b at peak 1 and peak 2 are 0.71 and 0.73, respectively; therefore, the kinetics for K_4PM are the combined effect of surface pseudocapacitive and diffusion behaviors. Further, the contribution of the above behaviors can be differentiated referring to the equation: $i = k_1v + k_2v^{1/2}$, where k_1v and $k_2v^{1/2}$ denote the current from the surface capacitive effect and diffusion-controlled process, respectively.^[24] As the typical example at the scan sweep of 0.2 mV s^{-1} (Figure S4), the surface capacitive-controlled contribution of K_4PM electrode is 28.1% for the K^+ ion storage. Correspondingly, as depicted in Figure 2c, the diffusion-controlled processes are still the

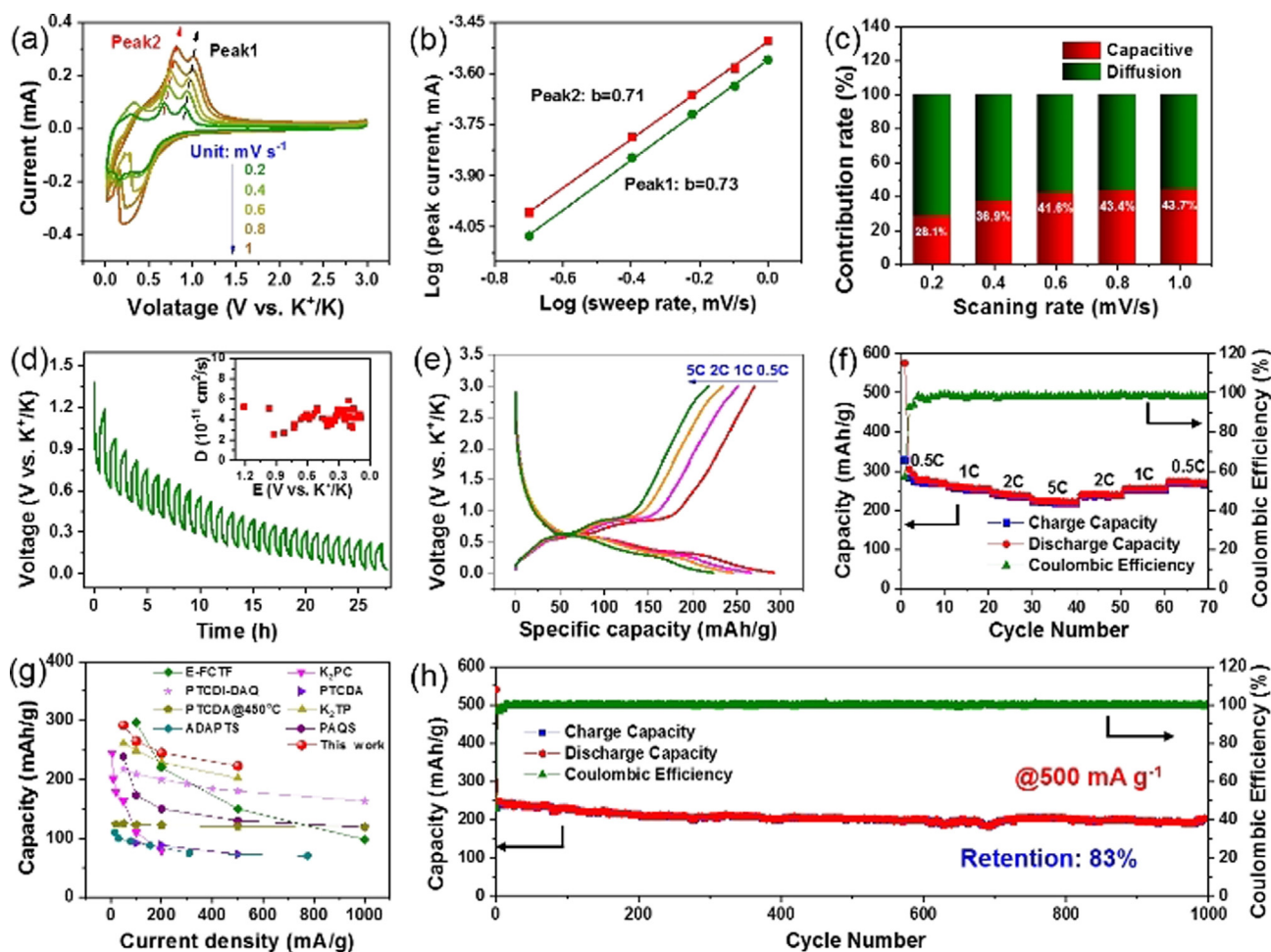


Figure 2. a) CV curves of K_4PM electrode for PIBs at different scan rates from 0.2–1 mVs^{-1} , b) Calculation of b values from the relationship between the scan rate and peak currents. c) The percent of pseudocapacitive contribution at different scan rates. d) Discharge GITT pattern of the K_4PM electrode, inset: the corresponding ion diffusion coefficient. e) Typical charge/discharge curves of different current densities. f) Rate performance. g) Comparison of rate performances between other K-organics cells and this work. h) Long-term cycling performance of K_4PM electrode at a current density of 500 $mA g^{-1}$.

main behaviors, although surface capacitive-controlled contributions increase up to 43.7% with the rise of scan sweeps. Further, the diffusion coefficient (D) of K^+ can be obtained by the galvanostatic intermittent titration technique (GITT in Figure 2d) based on Fick's second law:

$$D = 4/\pi\tau ((m_B V_M)/(M_B S))^2 / ((\Delta E_S)/(\Delta E_T))^2 \quad (1)$$

where τ is the pulse duration, m_B , M_B , and V_M are the active mass, molar mass, and molar volume of K_4PM , respectively, S is the surface area of the electrode, ΔE_S and ΔE_T are the voltage change caused by current pulse and by galvanostatic discharging, respectively.^[25] Here, the K_4PM electrode achieves a large diffusion coefficient (D) of K^+ ($\approx 4 \times 10^{-11} cm^2 s^{-1}$, inset of Figure 2d),^[26] which derives from the layered structure and large mesoporous volume. Next, the charge transfer kinetics between the electrolyte and electrodes can be tested by the electrochemical impedance spectroscopy (EIS) plots.^[27] As displayed in Figure S5, the charge transfer resistance (R_{CT}) of K_4PM electrode from the semi-circle in the low frequency range is $\approx 110 \Omega$, which is smaller

than the reported organic electrodes,^[13,28] further indicating the fast ion transfer in K_4PM . Meanwhile, the EIS plot of K_4PM after 1000 cycles was also tested, where the R_{CT} value is lower than that of the fresh K_4PM . The reduction of resistance after cycles is mainly ascribed to the activation process of K_4PM for potassium ion storage.

The discharge/charge profiles of K_4PM electrodes were depicted under the enhance current densities from 0.5 C to 5 C (Figure 2e, 1 C = 100 $mA g^{-1}$), where the K_4PM electrode displays two symmetric discharge/charge plateaus at 0.31/0.63 V and 0.54/0.89 V, respectively. The difference between discharge and charge plateaus is due to the battery polarizations. Meanwhile, it delivers the discharge specific capacities of ≈ 292 , 265, 245, and 223 $mAh g^{-1}$ at the current densities of 0.5 C, 1 C, 2 C, and 5 C with $\approx 100\%$ Coulombic efficiencies. Subsequently, the corresponding rate performances were evaluated (Figure 2f), where it regains a reversible capacity of $\approx 275 mAh g^{-1}$ after the current density is returned to 0.5 C, indicating the good reversibility, which is better than previously reported results of K-organic batteries (Figure 2g).^[13,14b,17b,18c,29] Further, the long-term cycling per-

performances of K_4PM electrode was tested at a high current density of 500 mA g^{-1} (Figure 2h), where its discharge capacities maintain over 205 mAh g^{-1} with the Coulombic efficiency of $\approx 100\%$ and a capacity retention of $\approx 83\%$ after 1000 cycles, among the best reported K-organics batteries (Table S1). And the discharge/charge plots under different cycles indicate the robust stability with nearly overlapped curves and voltage platforms, especially from 400th to 1000th cycles (Figure S6), which reveals the low electrode polarization and reversible redox behavior.

To explore the K^+ ion storage mechanism of K_4PM , we incorporated in situ and ex-situ characterizations to investigate the variations of functional groups and stability of crystal structure during the discharge/charge process. The in situ FT-IR spectra were measured in the range of 0.01–3 V to detect the evolution of functional groups of K_4PM during the potassiation/depotassiation process (Figures 3a and S6), where the background of data was based on the electrode and electrolyte (details in Supporting Information). During the potassiation process, the non-benzene $C=C$ vibration ($\nu(C=C)$) at $\approx 1656 \text{ cm}^{-1}$ emerges with the gradually enhanced intensities, along with the decrease of $\nu_{as}(-COO)$ and $\nu_s(-COO)$ (Figure 3b),^[17b] while the peak at 522 cm^{-1}

ascribed to $\nu(-KO)$ is split into two peaks at 528 and 515 cm^{-1} (Figure S7), which should be originated from the formation of new $K-O$ bond, indicating that the transition from conjugated carboxyls to enolates.^[11,17b] As for the depotassiation process, the peak at 1656 cm^{-1} weakened gradually, assigned to the recovery of non-benzene $C=C$ bonds into $C-C$ bonds with the enhancement of $\nu_{as}(-COO)$ and $\nu_s(-COO)$, and vibrations at 528 and 515 cm^{-1} receded with the increase of the peak at 522 cm^{-1} (Figure S7), suggesting the reversible transformation of the functional groups. Raman characterizations during the discharge/charge process also verified that the reversible evolution of conjugated carboxyls into enolates referring to the reversible decrease of $\nu_{as}(-COO)$ at 1567 cm^{-1} and $\nu_s(-COO)$ at 1370 cm^{-1} , and the reversible increase of $\nu(C=C)$ at $\approx 1656 \text{ cm}^{-1}$ (Figure 3c).^[26,30] XPS spectra further confirmed the reversible enolization reaction of the carbonyl group (Figures 3d,e, and S8), where the peak intensities of $C-O$ (peaks at 282.8 eV for $C 1s$ and 532.5 eV for $O 1s$) and $C=C$ (peak at 284.5 eV for $C 1s$) bonds are reversibly enhanced and peak intensity of $C=O$ (peaks at 288.2 eV for $C 1s$ and 530.9 eV for $O 1s$) bonds are reversibly weakened according to deconvolution results of $C1s$ and $O1s$ spectra^[31] during the discharge/charge process, which match well with the FT-IR

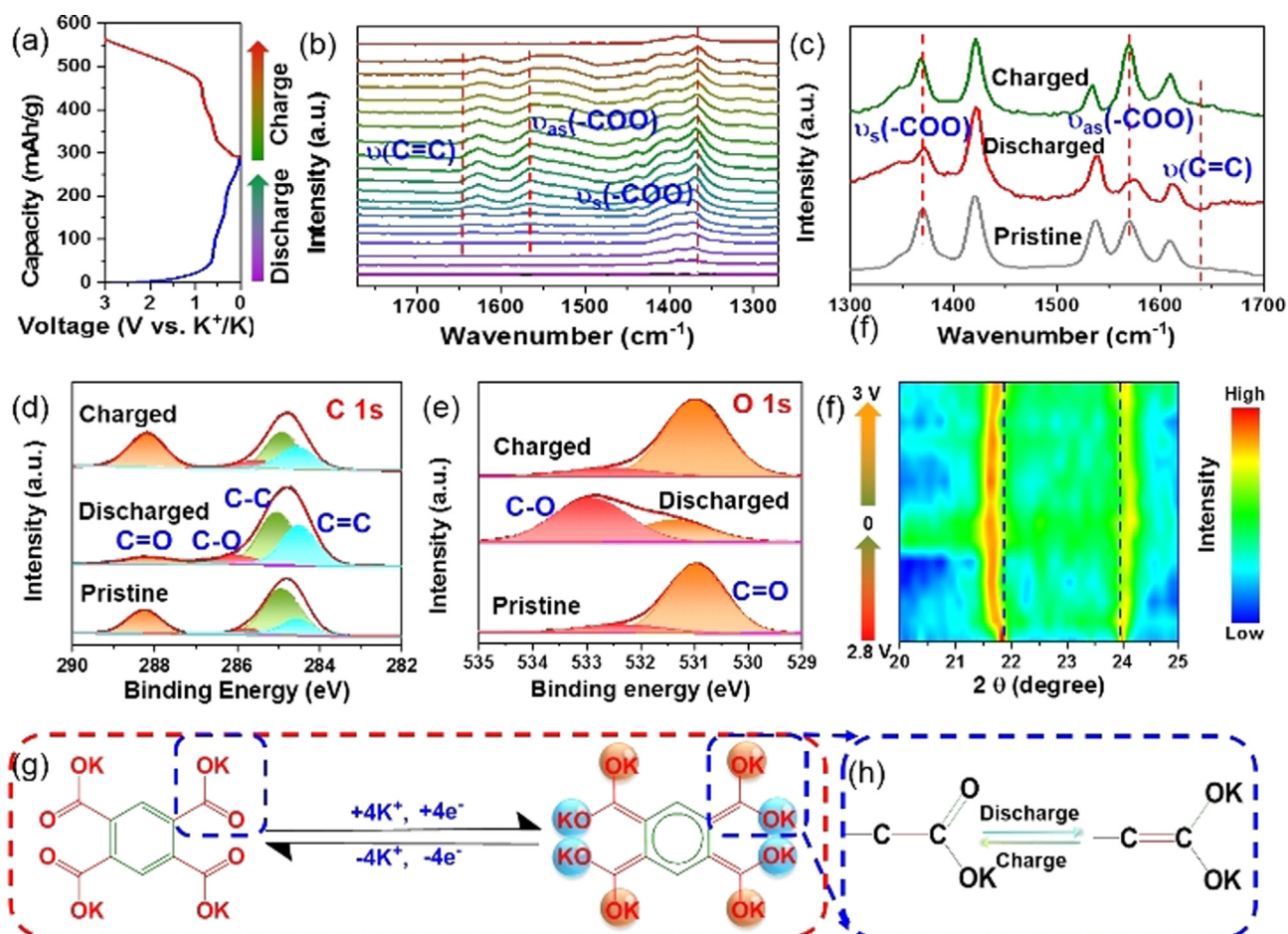


Figure 3. a) Typical discharge/charge curves. b) Corresponding spectra of in situ FT-IR, c) ex-situ Raman spectra, d) $C 1s$ and e) $O 1s$ spectra of ex-situ XPS spectra, and f) in situ XRD patterns. g) Proposed energy storage mechanism of K_4PM and corresponding variation of molecular structure during discharge/charge process.

and Raman results. Moreover, the diffraction peaks at $\approx 21.8^\circ$ and 24° reversibly shift to small angles and large angles in situ XRD patterns during the discharge/charge process, indicating the expansion and shrinkage of lattice planes owing to the accommodation of K^+ according to the Bragg equation: $2d\sin\theta = n\lambda$. After the charging process, the above two peaks recover gradually to the original states demonstrating remarkable structural stability. Based on the above investigations, the possible storage mechanism of K_4PM is illustrated in Figures 3 g and h, where the conjugated carboxyls are reversibly rearranged into enolates to accommodate K^+ ions with the structural reversibility during the discharge/charge process.

The first-principles density functional theory (DFT) calculations were further performed to understand the structural characteristic of K_4PM for potassium-ion storage. Figure 4a displays the diffusion processes of a K atom in the interlayer channels of K_4PM , where the highest diffusion energy barrier of K atom in K_4PM is only 0.322 eV (Figure 4b), which manifests that the K_4PM delivers a small diffusion resistance of K^+ ions^[32] due to the expanded interlayer distance (Figure 1e) than traditional graphite materials, in line with the EIS results (Figure S5) and contributing to the good rate performance (Figure 2e).^[33] Subsequently, the electronic properties of K_4PM were investigated by evaluating the variations of total density of states associated with K-atom intercalation into K_4PM . As demonstrated in Figure 4c, the pristine K_4PM possesses typical organic semiconductor properties with large band gaps. After introducing a single K-atom, its Fermi level (E_f) shifts to the conduction band edge, indicating the transition to the n-type semiconductor state upon K intercalation, conducive to the structural conductivity and the decrease of electrode impedance.^[34] Further, the charge density difference of K_4PM on K intercalation was investigated as shown in Figure 4d. The charge depletion centers (cyan) are the intercalated K atoms, and the partial charge accumulation centers (yellow) could be

dispersed on the benzene ring, similar to that of graphite with delocalized π bonds,^[35] manifesting potential structural stability and electronic conductivity. All these simulations demonstrate that K_4PM can accommodate K^+ ions with good ion diffusivity, fine electronic conductivity and robust stability, contributing excellent electrochemical performances.

In summary, we synthesized a laminar K_4PM electrode for potassium ion storage based on a design strategy, where organics are devised with small molecular mass, rich active sites, fast ion diffusion channels, and rigid conjugated π bonds. The K_4PM delivered expected performances for its abundant K^+ ion storage sites and large interlayer distance. It exhibited a high capacity of $\approx 290 \text{ mAh g}^{-1}$, good rate performance and excellent cycling stability with a capacity retention of $\approx 83\%$ after 1000 cycles. Further, DFT simulations incorporating with in situ and ex-situ techniques revealed that the K_4PM demonstrates a robust structural stability and the conjugated carboxyls are reversibly rearranged into enolates to accept K^+ ions during the discharge/charge process. We believe that this study may pave the way for rational design and synthesis of ideal organics for high-performance PIBs.

Acknowledgements

The authors gratefully acknowledge financial support from the Key Area Research and Development Program of Guangdong Province (2019B090914003), National Natural Science Foundation of China (51822210, 51972329, 52061160484, 22005330), China Postdoctoral Science Foundation (2020M672871), Shenzhen Science and Technology Planning Project (JCYJ20190807171803813, JCYJ20200109115624923), and Science and Technology Planning Project of Guangdong Province (2019TX05L389, 2018A050506066).

Conflict of interest

The authors declare no conflict of interest.

Keywords: battery · carboxyls · organic electrode · potassium · tetrapotassium pyromellitic

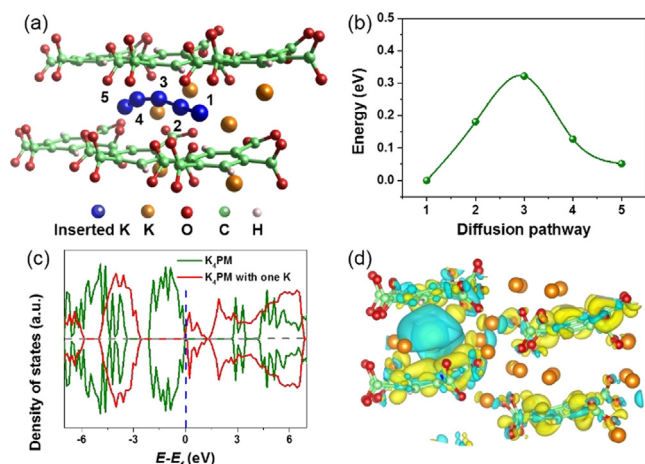


Figure 4. DFT simulations of K_4PM for potassium ion storage. a) Diffusion pathways and b) corresponding energy barriers of K^+ ions in K_4PM . c) Total density of states of K_4PM before and after inserting one K. d) Charge density difference of K_4PM after one K atom inserting, cyan: charge depletion; yellow: charge accumulation.

- [1] a) E. Pomerantseva, F. Bonaccorso, X. Feng, Y. Cui, Y. Gogotsi, *Science* **2019**, *366*, 969–981; b) D. Gong, C. Wei, Z. Liang, Y. Tang, *Small Sci.* **2021**, DOI: 10.1002/smssc.202100014; c) L.-L. Jiang, C. Yan, Y.-X. Yao, W. Cai, J.-Q. Huang, Q. Zhang, *Angew. Chem. Int. Ed.* **2021**, *60*, 3402–3406; *Angew. Chem.* **2021**, *133*, 3444–3448.
- [2] a) J.-Y. Hwang, S.-T. Myung, Y.-K. Sun, *Adv. Funct. Mater.* **2018**, *28*, 1802938; b) H. Yin, C. Han, Q. Liu, F. Wu, F. Zhang, Y. Tang, *Small* **2021**, DOI: 10.1002/smll.202006627; c) G. Zhang, X. Ou, C. Cui, J. Ma, J. Yang, Y. Tang, *Adv. Funct. Mater.* **2019**, *29*, 1806722; d) X. Zhou, Q. Liu, C. Jiang, B. Ji, X. Ji, Y. Tang, H.-M. Cheng, *Angew. Chem. Int. Ed.* **2020**, *59*, 3802–3832; *Angew. Chem.* **2020**, *132*, 3830–3861; e) T. Song, W. Yao, P. Kiadkhunthod, Y. Zheng, N. Wu, X. Zhou, S. Tunmee, S. Sattayaporn, Y. Tang, *Angew. Chem. Int. Ed.* **2020**, *59*, 740–745; *Angew. Chem.*

- 2020, 132, 750–755; f) S. Zhang, A. A. Teck, Z. Guo, Z. Xu, M.-M. Titirici, *Batteries Supercaps* **2021**, <https://doi.org/10.1002/batt.202000306>.
- [3] a) Q. Pan, D. Gong, Y. Tang, *Energy Storage Mater.* **2020**, *31*, 328–343; b) C. Jiang, X. Meng, Y. Zheng, J. Yan, Z. Zhou, Y. Tang, *CCS Chem.* **2021**, *3*, 85–94; c) M. Wang, Q. Liu, G. Wu, J. Ma, Y. Tang, *Green Energy Environ.* **2021**, <https://doi.org/10.1016/j.gee.2021.1003.1007>; d) Y. Lan, W. Yao, X. He, T. Song, Y. Tang, *Angew. Chem. Int. Ed.* **2020**, *59*, 9255–9262; *Angew. Chem.* **2020**, *132*, 9342–9349.
- [4] a) Y. Wu, H. Zhao, Z. Wu, L. Yue, J. Liang, Q. Liu, Y. Luo, S. Gao, S. Lu, G. Chen, X. Shi, B. Zhong, X. Guo, X. Sun, *Energy Storage Mater.* **2021**, *34*, 483–507; b) X. Li, X. Ou, Y. Tang, *Adv. Energy Mater.* **2020**, *10*, 2002567; c) J. Wang, H. Wang, X. Zang, D. Zhai, F. Kang, *Batteries Supercaps* **2021**, <https://doi.org/10.1002/batt.202000239>; d) Y. Xu, C. Zhang, M. Zhou, Q. Fu, C. Zhao, M. Wu, Y. Lei, *Nat. Commun.* **2018**, *9*, 1720.
- [5] F. Ming, H. Liang, G. Huang, Z. Bayhan, H. N. Alshareef, *Adv. Mater.* **2020**, *32*, 2004039.
- [6] Q. Yun, L. Li, Z. Hu, Q. Lu, B. Chen, H. Zhang, *Adv. Mater.* **2020**, *32*, 1903826.
- [7] a) J. Wu, Q. Zhang, S. Liu, J. Long, Z. Wu, W. Zhang, W. K. Pang, V. Sencadas, R. Song, W. Song, J. Mao, Z. Guo, *Nano Energy* **2020**, *77*, 105118; b) H. Liu, X. B. Cheng, J. Q. Huang, S. Kaskel, S. L. Chou, H. S. Park, Q. Zhang, *ACS Mater. Lett.* **2019**, *1*, 217–229.
- [8] Y. Wu, H.-B. Huang, Y. Feng, Z.-S. Wu, Y. Yu, *Adv. Mater.* **2019**, *31*, 1901414.
- [9] a) N. Wu, X. Zhou, P. Kidkhunthod, W. Yao, T. Song, Y. Tang, *Adv. Mater.* **2021**, DOI: 10.1002/adma.202101788; b) Q. Liu, H. Wang, C. Jiang, Y. Tang, *Energy Storage Mater.* **2019**, *23*, 566–586; c) C. Zhang, H. Zhao, Y. Lei, *Energy Environ. Mater.* **2020**, *3*, 105–120.
- [10] a) S. Liu, L. Kang, S. C. Jun, *Adv. Mater.* **2021**, *33*, 2004689; b) J. Xie, Q. Zhang, *Small* **2019**, *15*, 1805061; c) X. Cui, H. Dong, S. Chen, M. Wu, Y. Wang, *Batteries Supercaps* **2021**, *4*, 72–97; d) L. Zhang, H. Wang, X. Zhang, Y. Tang, *Adv. Funct. Mater.* **2021**, *31*, 2010958; e) X. Zhang, P. Don, M.-K. Song, *Batteries Supercaps* **2019**, *2*, 591–626.
- [11] L. Zhu, G. Ding, L. Xie, X. Cao, J. Liu, X. Lei, J. Ma, *Chem. Mater.* **2019**, *31*, 8582–8612.
- [12] X. Liu, Z. Ye, *Adv. Energy Mater.* **2020**, *10*, 2003281.
- [13] Y. Liang, C. Luo, F. Wang, S. Hou, S.-C. Liou, T. Qing, Q. Li, J. Zheng, C. Cui, C. Wang, *Adv. Energy Mater.* **2019**, *9*, 1802986.
- [14] a) Z. Q. Tong, S. Tian, H. Wang, D. Shen, R. Yang, C. S. Lee, *Adv. Funct. Mater.* **2020**, *30*, 10; b) J. Xie, P. Gu, Q. Zhang, *ACS Energy Lett.* **2017**, *2*, 1985–1996; c) C. Zhang, Y. Xu, K. He, Y. Dong, H. Zhao, L. Medenbach, Y. Wu, A. Balducci, T. Hannappel, Y. Lei, *Small* **2020**, *16*, 2002953.
- [15] T. Sun, J. Xie, W. Guo, D.-S. Li, Q. Zhang, *Adv. Energy Mater.* **2020**, *10*, 1904199.
- [16] C. Li, K. Wang, J. Li, Q. Zhang, *Nanoscale* **2020**, *12*, 7870–7874.
- [17] a) R. Rajagopalan, Y. Tang, X. Ji, C. Jia, H. Wang, *Adv. Funct. Mater.* **2020**, *30*, 1909486; b) K. Lei, F. Li, C. Mu, J. Wang, Q. Zhao, C. Chen, J. Chen, *Energy Environ. Sci.* **2017**, *10*, 552–557.
- [18] a) Q. Zhang, W. Zhang, W. Huang, *Chem. Eur. J.* **2020**, <https://doi.org/10.1002/chem.202005295>; b) L. Fan, R. F. Ma, J. Wang, H. G. Yang, B. A. Lu, *Adv. Mater.* **2018**, *30*, 1805486; c) J. Xie, W. Chen, G. Long, W. Gao, Z. J. Xu, M. Liu, Q. Zhang, *J. Mater. Chem. A* **2018**, *6*, 12985–12991.
- [19] a) H. S. Cahyadi, W. William, D. Verma, S. K. Kwak, J. Kim, *ACS Appl. Mater. Interfaces* **2018**, *10*, 17183–17194; b) M. A. Silva, N. R. de Campos, L. A. Ferreira, L. S. Flores, J. C. A. Júnior, G. L. dos Santos, C. C. Corrêa, T. C. dos Santos, C. M. Ronconi, M. V. Colaço, T. R. G. Simões, L. F. Marques, M. V. Marinho, *Inorg. Chim. Acta* **2019**, *495*, 118967.
- [20] a) R. Diniz, H. A. De Abreu, W. B. De Almeida, N. G. Fernandes, M. T. C. Sansiviero, *Spectrochim. Acta Part A* **2005**, *61*, 1747–1757; b) C. H. J. Franco, W. R. do Carmo, F. B. de Almeida, H. A. de Abreu, R. Diniz, *Struct. Chem.* **2015**, *26*, 773–783.
- [21] H.-J. Liang, B.-H. Hou, W.-H. Li, Q.-L. Ning, X. Yang, Z.-Y. Gu, X.-J. Nie, G. Wang, X.-L. Wu, *Energy Environ. Sci.* **2019**, *12*, 3575–3584.
- [22] R. Xu, L. Du, D. Adekoya, G. Zhang, S. Zhang, S. Sun, Y. Lei, *Adv. Energy Mater.* **2020**, *10*, 2001537.
- [23] a) X. Chang, X. Zhou, X. Ou, C.-S. Lee, J. Zhou, Y. Tang, *Adv. Energy Mater.* **2019**, *9*, 1902672; b) K. Yang, Q. Liu, Y. Zheng, H. Yin, S. Zhang, Y. Tang, *Angew. Chem. Int. Ed.* **2021**, *60*, 6326; *Angew. Chem.* **2021**, *133*, 6396.
- [24] P. Simon, Y. Gogotsi, B. Dunn, *Science* **2014**, *343*, 1210–1211.
- [25] Z.-Y. Gu, Z.-H. Sun, J.-Z. Guo, X.-X. Zhao, C.-D. Zhao, S.-F. Li, X.-T. Wang, W.-H. Li, Y.-L. Heng, X.-L. Wu, *ACS Appl. Mater. Interfaces* **2020**, *12*, 47580–47589.
- [26] A. Yu, Q. Pan, M. Zhang, D. Xie, Y. Tang, *Adv. Funct. Mater.* **2020**, *30*, 2001440.
- [27] a) Q. Pan, K. Yang, G. Wang, D. Li, J. Sun, B. Yang, Z. Zou, W. Hu, K. Wen, H. Yang, *Chem. Eng. J.* **2019**, *372*, 399–407; b) Q. Pan, T. Chen, L. Ma, G. Wang, W. B. Hu, Z. Zou, K. Wen, H. Yang, *Chem. Mater.* **2019**, *31*, 8062–8068; c) S. Peng, X. Zhou, S. Tunmee, Z. Li, P. Kidkhunthod, M. Peng, W. Wang, H. Saitoh, F. Zhang, Y. Tang, *ACS Sustainable Chem. Eng.* **2021**, <https://doi.org/10.1021/acssuschemeng.1020c08119>; d) Q. Xiong, G. Huang, X.-B. Zhang, *Angew. Chem. Int. Ed.* **2020**, *59*, 19311–19319; *Angew. Chem.* **2020**, *132*, 19473–19481.
- [28] P. Xiao, S. Li, C. Yu, Y. Wang, Y. Xu, *ACS Nano* **2020**, *14*, 10210–10218.
- [29] a) Q. Deng, J. Pei, C. Fan, J. Ma, B. Cao, C. Li, Y. Jin, L. Wang, J. Li, *Nano Energy* **2017**, *33*, 350–355; b) H. Zhang, W. Sun, X. Chen, Y. Wang, *ACS Nano* **2019**, *13*, 14252–14261; c) Y. Chen, W. Luo, M. Carter, L. Zhou, J. Dai, K. Fu, S. Lacey, T. Li, J. Wan, X. Han, Y. Bao, L. Hu, *Nano Energy* **2015**, *18*, 205–211; d) Y. Hu, W. Tang, Q. Yu, X. Wang, W. Liu, J. Hu, C. Fan, *Adv. Funct. Mater.* **2020**, *30*, 2000675.
- [30] Y. Luo, L. Liu, K. Lei, J. Shi, G. Xu, F. Li, J. Chen, *Chem. Sci.* **2019**, *10*, 2048–2052.
- [31] a) X. Lei, Y. Zheng, F. Zhang, Y. Wang, Y. Tang, *Energy Storage Mater.* **2020**, *30*, 34–41; b) L. Fan, R. Ma, Q. Zhang, X. Jia, B. Lu, *Angew. Chem. Int. Ed.* **2019**, *58*, 10500–10505; *Angew. Chem.* **2019**, *131*, 10610–10615.
- [32] J. Lang, J. Li, X. Ou, F. Zhang, K. Shin, Y. Tang, *ACS Appl. Mater. Interfaces* **2020**, *12*, 2424–2431.
- [33] C. Heubner, K. Nikolowski, S. Reuber, M. Schneider, M. Wolter, A. Michaelis, *Batteries Supercaps* **2021**, *4*, 268–285.
- [34] a) S. Ghosh, M. A. Makeev, M. L. Macaggi, Z. Qi, H. Wang, N. N. Rajput, S. K. Martha, V. G. Pol, *Mater. Today Energy* **2020**, *17*, 100454; b) C. Jiang, Y. Fang, W. Zhang, X. Song, J. Lang, L. Shi, Y. Tang, *Angew. Chem. Int. Ed.* **2018**, *57*, 16370–16374; *Angew. Chem.* **2018**, *130*, 16608–16612.
- [35] a) S. Zeng, X. Chen, R. Xu, X. Wu, Y. Feng, H. Zhang, S. Peng, Y. Yu, *Nano Energy* **2020**, *73*, 104807; b) F. J. Sonia, M. K. Jangid, M. Aslam, P. Johari, A. Mukhopadhyay, *ACS Nano* **2019**, *13*, 2190–2204.

Manuscript received: March 1, 2021

Accepted manuscript online: March 15, 2021

Version of record online: April 13, 2021